Automatic Design Optimisation of a Transonic Compressor Rotor for Improving Aeroacoustic and Aerodynamic Performance

Long Wu*
Research Fellow
Email: longwu777@gmail.com, L.Wu@soton.ac.uk
Jae Wook Kim
Professor of Aerodynamics and Aeroacoustics
Email: J.W.Kim@soton.ac.uk
Alexander George Wilson
Professor in Computational Aeroacoustics
Email: A.G.Wilson@soton.ac.uk

Institute of Sound and Vibration Research
University of Southampton
Southampton, SO17 1BJ, United Kingdom

Shahrokh Shahpar
Rolls-Royce Engineering Fellow – Aerothermal Design System
Email: Shahrokh.Shahpar@Rolls-Royce.com

Innovation Hub, Future Methods
Rolls-Royce plc.
Derby, DE24 8BJ, United Kingdom

Multidisciplinary design optimisation of transonic rotors, especially focusing on improving the aeroacoustic performance, has received little attention. This paper employs an automatic design optimisation approach to reduce the shock-associated tone noise and to increase the adiabatic efficiency of NASA rotor 37. An evolutionary algorithm for multi-objective trade-offs searching is used to obtain the noise-efficiency Pareto front. Three-dimensional Reynolds averaged Navier-Stokes simulations are directly applied in the optimisation loop for aeroacoustic and aerodynamic analysis. Significant noise reduction and efficiency increase have been achieved. Two optimised designs corresponding to the endpoints of the Pareto front have been analysed comprehensively from the perspectives of rotor characteristics, noise performance, and flow and acoustic fields, to understand the mechanisms responsible for the performance improvements.

*Address all correspondence to this author.

1 Introduction

On the route to environmentally friendly and climate neutral transport systems, a continued effort in optimisation of aircraft engines is required for a further reduction of carbon-dioxide and noise emissions of the aviation sector. Reducing the environmental footprint of aviation remains an essential target for aircraft engine manufacturers, therefore. With all the achieved noise reductions over the past decades in modern high bypass ratio turbofan engines, the fan noise remains to have a major contribution to the overall engine noise at all operating conditions. Application of advanced acoustic liner technologies in the engine nacelle for reduced propagation is limited by the associated weight and drag impact. Therefore, there is a growing requirement to reduce the source level of the fan noise during the blade design phase. Meanwhile, the demands of high pressure ratio and high efficiency are consistently increasing for lighter weight and better fuel economy.

The fan of an aircraft engine usually operates in the transonic regime during take-off and climb. A "rotor-locked" shock field, that is rotating together with the rotor, is formed and propagates upstream helically along the engine duct in

the stationary frame of reference. The strength of the wave system decays with the distance from the blades as a result of nonlinearity and dissipation during the in-duct propagation. However, acoustic modes of lower-order circumferential Fourier harmonics of the flow field can escape out of the engine duct and radiate to the far-field, due to their cut-on nature at supersonic relative speeds [1]. This results in a noise spectrum characterised by a combination of strong discrete tones at frequencies which are integer multiples of the rotor rotation frequency, i.e., engine orders (EO). For an ideal rotor of identical blades in a circumferentially uniform incoming flow, only EO tones at the blade passing frequency (BPF) and its harmonics would be produced [1, 2]. In practice, due to minor blade-to-blade variations of manufacturing and installation, an irregular circumferential pattern, of which a complete repetition occurs once per rotor revolution, is assembled by the shock and expansion waves arising from each blade. As a result, many more EO tones at multiples of the shaft rotation frequency are observed, which are generally referred as multiple pure tones or buzz-saw noise [3].

At the same time, it is known that for transonic rotors the high pressure rise is mainly achieved by the strong compression process across the blade passage shock. However, shock waves are also responsible for significant loss mechanisms in transonic rotors [4]. Not only the shock loss is generated due to direct entropy production across the shock, but also, indirectly, viscous losses are increased because the shock-boundary layer interaction would result in boundary layer thickening and possibly flow separation. Besides, other complex flow structures in a transonic rotor such as tip leakage flow, endwall secondary flow, and radial migration of near-wall flow, all together bring great challenges for the design of transonic rotors.

Driven by the requirement to reduce the time cost for the design cycle, automatic multidisciplinary design optimisation (MDO) has attracted great attention in recent decades. It strongly complements the traditional, design-by-analysis approach in the field of turbomachinery blade design. A set of optimal compromises between competing objectives from different disciplines, i.e., the Pareto front, is often desired for an MDO problem rather than a single solution because the Pareto front can provide more information and choices to the designers. Multi-objective genetic algorithm (MOGA) as well as its variants [5, 6] has become the standard approach for trade-offs searching, by which a set of design solutions is directly evolved during the optimisation. In the practices of turbomachinery blade design, MOGA is often combined with response surface modelling [7–9] to reduce the time cost of the optimisation.

Previous investigations [10–15] on the optimisation of transonic rotors mostly contributed to the aerodynamic design and aero-mechanical design. To the authors' knowledge, the only MDO work for transonic rotors particularly targeting the reduction of aerodynamic noise was developed in [16], in which a low tone noise transonic fan blade was designed and tested. Instead of adopting the automatic design method, they first conducted a Taguchi design of experiments (DOE) on a 9-parameter design space to provide an initial low noise geometry. Then, a gradient-based optimisation to reduce the noise cost function, with the aerodynamic and mechanical properties treated as constraints, was performed on a 5-parameter design space, which was specified to only perturb the chordwise leading-edge sweep of the upper portion of the fan blade. The effects of the intake liner and the fan operating points on the low-noise design optimisation were specially highlighted.

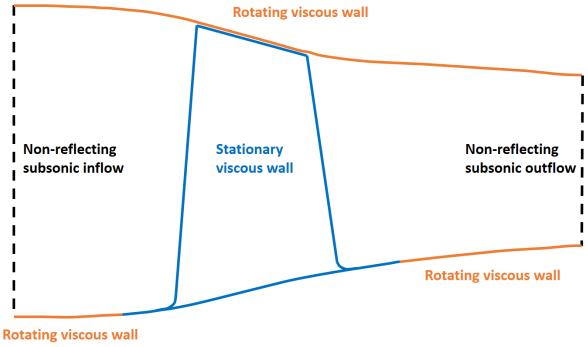

Fig. 1: Computational domain and boundary conditions

It is of great need to put more research efforts into the MDO of transonic rotors with the low noise goal considered. In this context, aeroacoustic and aerodynamic design optimisation of a transonic rotor is developed in the present paper. The aim is to reduce the shock-associated tone noise and to increase the aerodynamic performance of the rotor. Three-dimensional Reynolds averaged Navier-Stokes (RANS) simulations are directly used in the optimisation. The adaptive range multi-objective genetic algorithm (ARMOGA) [6, 17] is used to generate the Pareto front for the aeroacoustic-aerodynamic trade-offs analysis.

2 Case Description and Numerical Framework

2.1 Case Configuration

The case used in the present study is NASA rotor 37, which has been extensively used for turbomachinery CFD validations [18–20]. The aerodynamic design parameters and detailed experimental data of NASA rotor 37 are documented in [20–22]. The design rotation speed is 1800rad/s. It is a single-row, highly loaded, transonic rotor consisting of 36 blades, and is still a challenging case for today's CFD simulations due to strong interactions between complex flow structures. To the best of the authors' knowledge, there may not have been an attempt to improve the aeroacoustic performance of NASA rotor 37 by design optimisation, while much progress has been made previously on its aerodynamic [10, 11] and aero-mechanical [13, 14] optimisation.

The "rotor-locked" nature of the shock-associated tone noise permits that the noise and the aerodynamic performance of transonic rotors can be predicted simultaneously based on a steady CFD solution in the rotating frame of reference. In this study, a single blade passage of NASA rotor 37 is used to define the computational domain, as shown in

Fig. 1. The steady flow calculations are performed by solving the RANS equations with the Spalart-Allmaras turbulence model. The CFD boundary conditions are also given in Fig. 1, with non-reflecting characteristic boundary conditions applied on both the rotor inlet and outlet. The total pressure, total temperature, and inflow angles are specified on the rotor inlet. A fixed value of exit flow function together with the radial equilibrium equation is enforced on the outlet boundary, which will be further discussed in Sec. 4.1.2. Periodic boundary conditions are used circumferentially for the single passage domain.

The choice of this single-blade-passage configuration is made according to the following considerations. First, a full annulus CFD simulation and a geometric parameterisation to model the actual blade-to-blade variations would be inevitable if buzz-saw noise was directly targeted. However, it is almost prohibitive to apply such an expensive configuration in the optimisation for low-noise blade design. Second, the spectral evolution of buzz-saw noise along the rotor axis can be attributed to the nonlinear propagation of shock waves [23]. Initially, the small differences between the rotor blades would generate an almost regular saw-tooth pattern, i.e., shocks of slightly different strengths or positions, in front of the rotor. Hence, the noise spectrum measured very close to the rotor would be dominated by rotor BPF harmonics. Because the speed of each shock is determined by its strength, these shocks would chase and catch each other during their propagation. Some of them would merge. This nonlinear process would enhance the irregularity of the saw-tooth pattern, and consequently, transfer the acoustic spectral energy from the BPF tones to the other EO tones as shocks propagate upstream. Therefore, it is physically reasonable to focus on reducing the BPF tones, while buzz-saw noise of the rotor in practice could be expected to decrease as well [16]. In conclusion, the aeroacoustic objective of NASA rotor 37 will be defined based on those rotor-alone tones at BPF harmonics, for which a single blade passage domain is adequate.

2.2 Numerical Flow Solver and Noise Modelling

The numerical solver for steady RANS simulations in the present study is the Rolls-Royce HYDRA code [24]. It is a general-purpose CFD solver for hybrid unstructured meshes using an efficient edge-based data structure. A MUSCL-based flux-differencing algorithm is used for spatial discretization. An explicit Runge-Kutta pseudo-time-marching scheme is used to iterate the discrete flow equations towards the steady state. Convergence is accelerated using an element-collapsing multigrid algorithm. The code is parallelized based on domain decomposition.

After a steady RANS solution is obtained, a waves-splitting approach [25, 26] based on eigenanalysis is applied to decompose the rotor upstream flow field into upstream and downstream travelling eigenmodes. Then the shock-associated noise can be extracted in the form of modal components at each circumferential and radial harmonic.

Sound power over an axial cross section S of the duct can be well approximated using the sound intensity formula proposed in [27],

$$\boldsymbol{I}(\boldsymbol{x}_s,t) = (p' + \rho_0 \boldsymbol{u}' \cdot \boldsymbol{u}_0)(\boldsymbol{u}' + \frac{p'}{\gamma p_0}\boldsymbol{u}_0), \tag{1}$$

where p' and $\boldsymbol{u}'$ are fluctuations of static pressure and the velocity vector, ρ_0, p_0, and $\boldsymbol{u}_0$ are time-averaged flow density, static pressure, and the velocity vector, and γ is the ratio of specific heats for an ideal gas. The total sound power level (*PWL*) at a fixed axial location is calculated in cylindrical coordinate system by

$$PWL(x) = 120 + 10\log_{10}\left\{\frac{1}{T}\int_T \left[\iint_S \left|I_x(x,r,\theta,t)\right| r dr d\theta\right] dt\right\}. \tag{2}$$

Here, I_x is the axial component of the sound intensity vector, and T is the period for time averaging. Equation (1) and (2) can be also applied in frequency domain to determine the *PWL* of each acoustic eigenmode.

2.3 Mesh Generation

The mesh is generated using the Rolls-Royce PADRAM code [28]. An H-O-H grid topology is applied to the blade-to-blade section, and a distribution of radial grid points clustering toward the hub and the casing walls is used for the spanwise stacking. The blade tip gap is gridded using a "butterfly" topology, and the radial grid points within the gap are clustered toward two ends as well. A large number of grid points in the upstream H (USH) block are required to resolve the acoustic waves of the rotor BPF tones. Uniform distributions of the axial and circumferential grids are adopted for the USH mesh, and it has an estimated resolution of 20 points per theoretical wavelength for the 3BPF harmonic. This ensures the wave amplitude decay caused by the numerical dissipation [29] for the frequencies of interest is negligible compared with the nonlinear decay. The maximum radial grid spacing is restricted to be small enough to resolve the radial shape of the least cut-on acoustic mode for the frequencies of interest. The final mesh used for the present study consists of 7.16 million cells, and the detailed numbers of grid points are given in Tab. 1. The y^+ distribution around the blade and some mesh details are shown in Fig. 2.

3 Simulation Validation and Noise Analysis

3.1 Results of the Rotor Performance

The present numerical simulations are first validated by comparison of the rotor characteristics at the design speed with the experiment [22] and with other CFD results [30,31]. The choke mass flow rate found from the present simulations is 20.90kg/s, which is close to the experimental value of 20.93kg/s. It can be seen from Fig. 3 that the present simulations give an overall reasonable prediction of the rotor

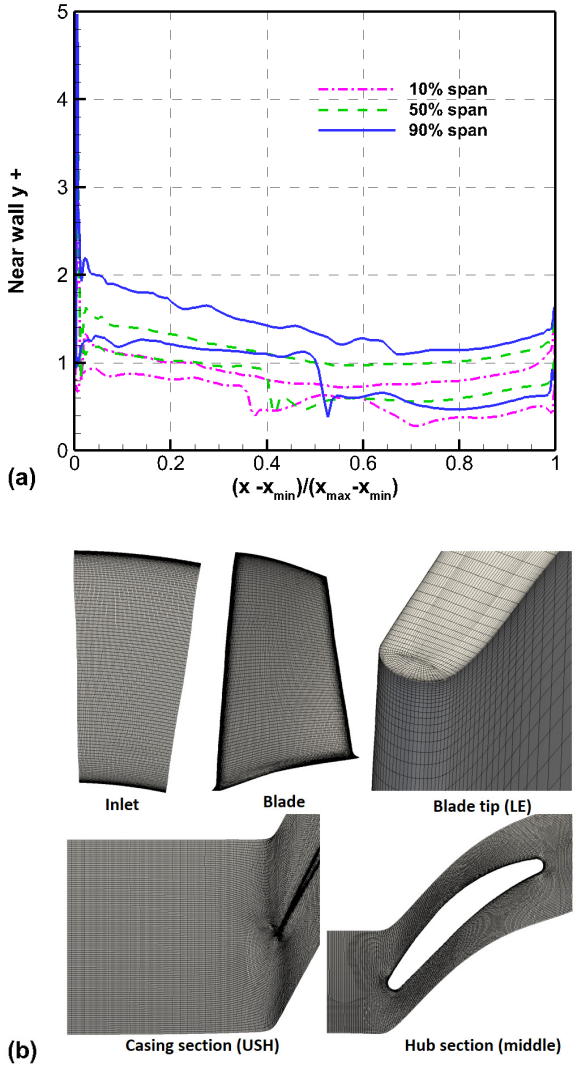

Fig. 2: (a) Near wall y^+ distributions around the blade at three spanwise locations, and (b) mesh details

characteristics. The trend of an under-predicted rotor efficiency agrees with the previous studies and has previously been attributed to the measurement uncertainty in the experiment [18,32]. Further comparisons of the spanwise profiles of total pressure ratio and adiabatic efficiency at the design point, i.e., 98% of the choke mass flow, are made in Fig. 4. The agreements between the present simulation and the experiment are satisfactory, despite a distinct discrepancy of total pressure ratio near the blade hub. This was investigated in previous studies [31,33], where a possible cause was speculated to be a lack of upstream hub cavity in numerical simulations. It can be inferred from the efficiency distribution that most of the efficiency losses are generated by the flow at above 20% span, especially near the blade tip region.

Table 1: Numbers of grid points

Number of points in radial direction	169
Number of points in radial direction, tip gap	27
Number of points in circumferential direction, USH	93
Number of points in axial direction	418
Number of points in axial direction, USH	180

3.2 Shock-associated tone noise

Figure 5 shows axial distributions of *PWL* of the first five radial modes and the total net power for 1BPF and 2BPF tones. Note the origin of the x coordinate is the leading edge of the blade hub section, and the mean chord of NASA rotor 37 is 0.0562m. The net acoustic power is mainly contributed by upstream propagating modes of each BPF harmonic. The *PWL* distribution of the fifth radial mode for 1BPF confirms that it becomes cut-off upstream of the location $x = -0.015$m, as a rapid (exponential) decay is observed. Figure 5 also shows some evidence of interactions between different radial modes due to the strong nonlinearity, as their proportions in the total acoustic power vary with the axial locations.

The overall decay trend of *PWL* towards the upstream direction is mainly due to the nonlinear nature of shock wave propagation. It is further examined in Fig. 6, where a least-squares fitted curve in the form of

$$PWL_{\text{fitted}}(x) = a10\log_{10}(|x - x_{\text{LE}}|) + C$$

is generated using the total *PWL* data directly obtained in the time domain. Here, a is the exponent of the power law that describes the nonlinear decay with the axial distance away from the rotor, and x_{LE} is chosen to be the average of axial coordinates of the leading edge at rotor hub and tip sections. A relation of $(x - x_{\text{LE}})^{-1.2}$ for sound power decay is found for the present case. It is stronger than the $(x - x_{\text{LE}})^{-1}$ near-field power decay inferred from the two-dimensional theory [23, 34], which suggests that radial re-distributions of the shock front caused by the changing of mode shapes might have the effect of intensifying the decay process. It can be also seen that the total net *PWL* of 2BPF harmonic is only about 6dB lower than that of 1BPF over the whole upstream range, which indicates the contribution of high-order BPF harmonics cannot be neglected. Therefore, it is decided to use the time-domain definition of the total *PWL* as the acoustic objective for optimisation.

4 Automatic Design Optimisation

In this section, the aeroacoustic and aerodynamic optimisation of NASA rotor 37 is carried out. First, the optimisation problem is introduced. Then the optimisation results are presented, and two representative designs are compared with the datum rotor in terms of the aerodynamic and aeroacoustic

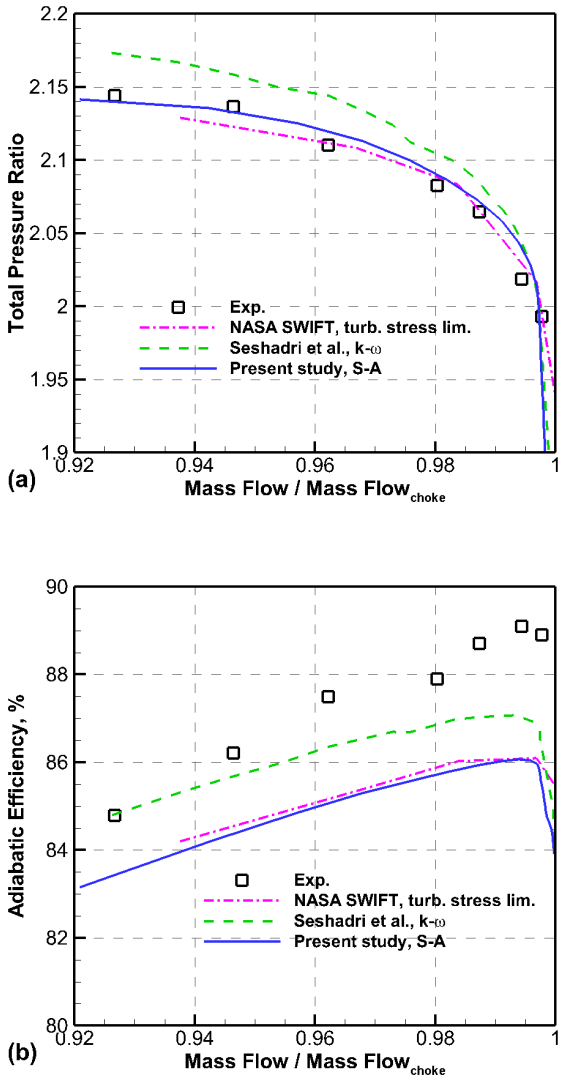

Fig. 3: Comparison of rotor performance curves of (a) total pressure ratio, and (b) adiabatic efficiency between the present results, experimental data [22], and other CFD results [30, 31] at 100% rotor speed

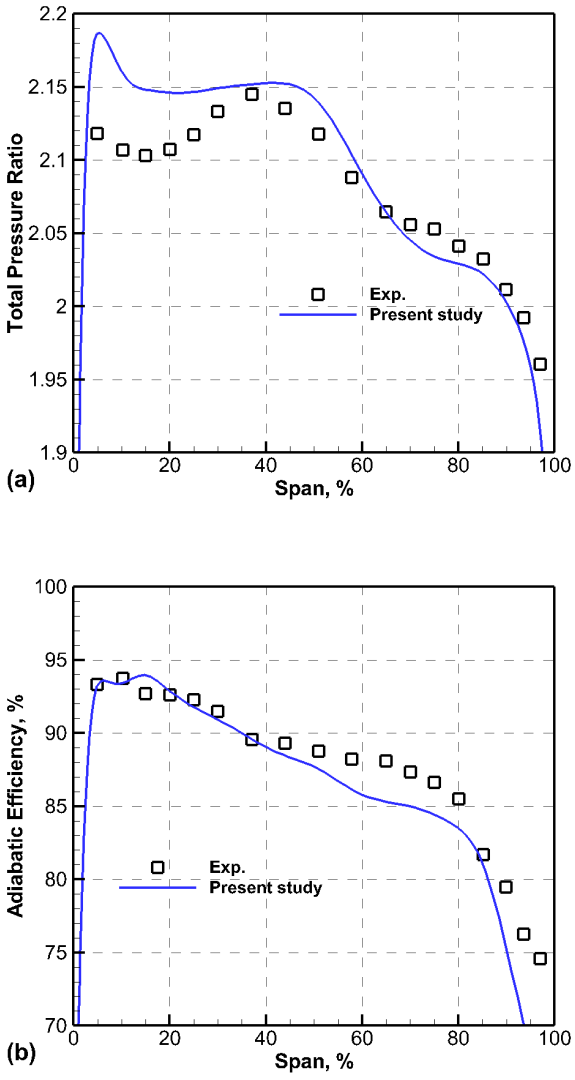

Fig. 4: Comparison of spanwise profiles of (a) total pressure ratio, and (b) adiabatic efficiency between the present results and experimental data [22] at the design point of NASA rotor 37

performance. Finally, some analyses of the flow and acoustic fields are made to understand the mechanisms responsible for the performance improvements.

4.1 Optimisation Problem

4.1.1 Blade Parameterisation

The rotor blade is parameterised by using engineering design parameters in the Rolls-Royce PADRAM code [28], which are summarised in Tab. 2. The five engineering parameters modify the sectional blade shape and are applied respectively at 20, 40, 60, 80 and 100% blade span locations. Piecewise cubic spline interpolation is used for the spanwise distribution of the engineering parameters. Figure 7 as an illustration shows the effects of each engineering parameter on reshaping the blade section. The main advantages of these engineering parameters are that they are intuitive to designers, and also do not change the blade thickness.

The design space of 25 design variables for the present optimisation is defined by setting the lower and upper bounds of the five engineering parameters for each of the five spanwise locations as follows,

$$\begin{cases} -5 \leq \mathrm{XCEN}_i \leq 5 \\ -1 \leq \mathrm{DELT}_i \leq 1 \\ -1 \leq \mathrm{SKEW}_i \leq 1, \; i = 1, 2, \cdots, 5. \\ -1 \leq \mathrm{LEMO}_i \leq 1 \\ -1 \leq \mathrm{TEMO}_i \leq 1 \end{cases} \tag{3}$$

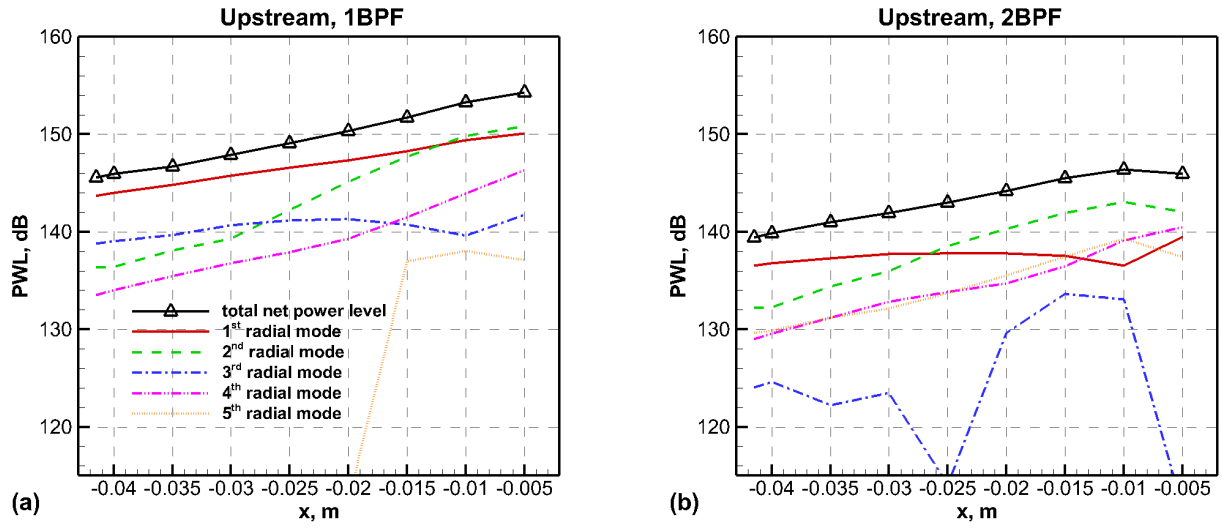

Fig. 5: Axial distributions of *PWL* in front of the rotor of (a) upstream modes for 1BPF and (b) upstream modes for 2BPF, with the distribution of total net power level for each BPF harmonic also plotted (all subplots share the same line legend)

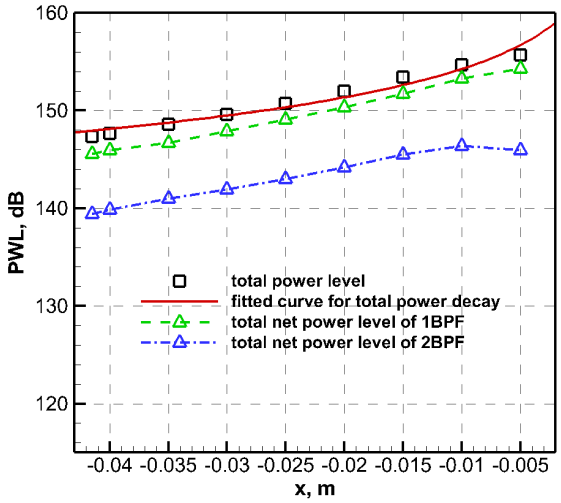

Fig. 6: Nonlinear decay of the acoustic power level

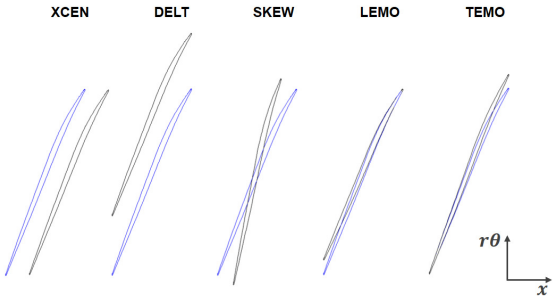

Fig. 7: Blade geometry reshaping using engineering parameters (blue: datum, black: design change applied)

Table 2: PADRAM engineering design parameters

XCEN	Axial sweep, mm
DELT	Circumferential lean, degree
SKEW	Re-staggering, degree
LEMO	Leading edge re-cambering, degree
TEMO	Trailing edge re-cambering, degree

4.1.2 Initial DOE Analysis

An initial design of experiments is conducted on the current design space using the optimal Latin hypercube method [35]. Three-dimensional RANS simulations are performed to predict the aerodynamic and aeroacoustic performance of NASA rotor 37 at 500 DOE points. 257 candidates among them are eliminated due to either breakdown of mesh generation or bad CFD convergence. Nonetheless, the remaining 243 DOE points can be regarded as a reasonable sampling of the design space, of which the distribution is almost even.

The DOE results for the aerodynamic and aeroacoustic performance of NASA rotor 37 are analysed. Figure 8(a)-(c) indicate there is a good chance to reduce the rotor noise and increase its efficiency simultaneously, but probably at the expense of the pressure ratio decrease. The data clustering and widening towards the direction of performance improvements imply the existence of trade-offs between the concerned performance parameters.

A strong, positive, linear correlation between the total pressure ratio and mass flow of the rotor is observed in Fig. 8(d). This is due to the use of a fixed value of the exit flow function for the outflow boundary condition, which is equivalent to imposing a constraint equation during the opti-

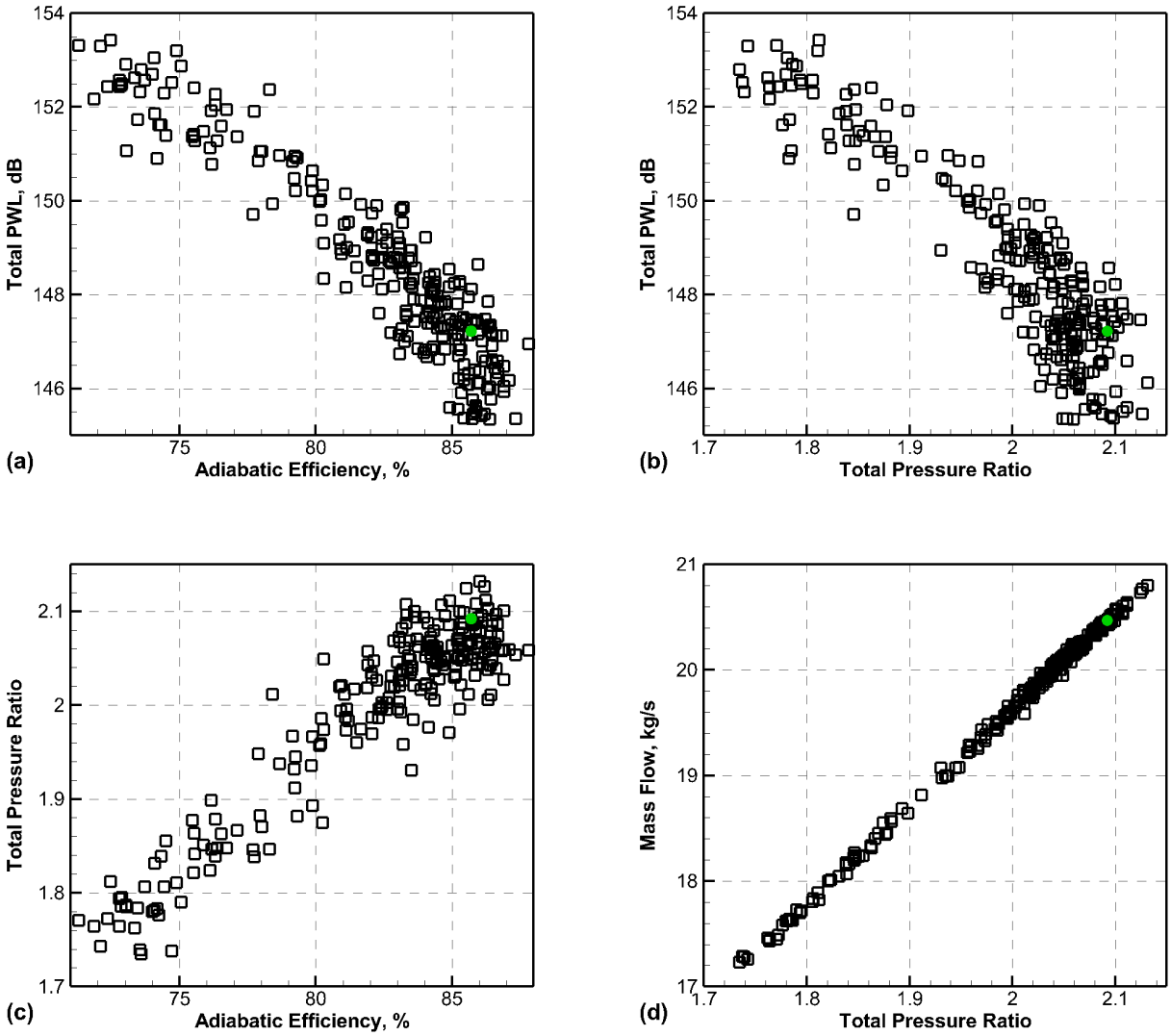

Fig. 8: DOE results of performance parameters (green dot: datum)

misation as follows,

$$\frac{\dot{m}\sqrt{TR}}{PR} = \frac{p^*_{\text{inlet}}}{\sqrt{T^*_{\text{inlet}}}} K A_{\text{exit}} q(M_{\text{exit}}). \tag{4}$$

Here, $\dot{m}$ is the mass flow, PR is the total pressure ratio, TR is the total temperature ratio, p^*_{inlet} is the inlet total pressure, T^*_{inlet} is the inlet total temperature, A_{exit} is the area of the exit cross section, $q(M_{\text{exit}})$ is the non-dimensional exit flow function, and K is a constant for a specific gas. As the variations of the rotor total temperature ratio are relatively small, Eqn. (4) almost degrades into a linear relationship between total pressure ratio and mass flow when $q(M_{\text{exit}})$ is fixed. This constraint equation, to some extent, effectively ensures that the optimisation is performed on a working line of the original rotor. Therefore, it is a reasonable simulation of the operating condition of a blade row in realistic, multi-stage compression configurations [31]. The value of $q(M_{\text{exit}})$ used for the optimisation is determined based on rotor performance parameters at the design point.

4.1.3 Optimisation Objectives and Algorithm

The goals of the present optimisation are to reduce the total PWL at the inlet and to increase the adiabatic efficiency η for NASA rotor 37. The optimisation problem is

$$\min : \{PWL(x_{\text{inlet}}), 1-\eta\}. \tag{5}$$

Except for the bounds of design variables in Eqn. (3) and ruling out failed CFD simulations, no constraint is imposed for the optimisation problem.

The optimisation algorithm used for the present work is the real-coded ARMOGA [6, 17]. It is an efficient method

for multi-objective trade-offs searching, as the search region is adaptively changed based on the population statistics of the average and the standard deviation. The optimisation process is automated by using the Rolls-Royce SOPHY system [36], in which the mesh generation, CFD simulation, and optimisation algorithm are integrated.

4.2 Optimisation Results

The size of the population used for each generation of the noise-efficiency optimisation is 250. The optimisation has been run for evolutions of 21 generations, and the 5250 numerical simulations have taken 8 weeks on a computer cluster of 864 CPU cores.

4.2.1 Pareto-Optimal Design Solutions

Figure 9 shows the noise-efficiency optimisation results at four different generations (the 6th, 11th, 16th, and 21st generations), as well as the results of all design candidates during the optimisation. Although the noise-efficiency Pareto fronts obtained at four generations in Fig. 9(a) indicate that the optimisation has not yet fully converged, noticeable noise reduction and efficiency increase have been achieved. Each design solution on the Pareto fronts has lower noise and higher efficiency compared with the datum blade. However, as can be seen in Fig. 9(b) and (c), these benefits for noise and efficiency are accompanied by pressure ratio decreases (or equivalently, mass flow decreases) to different extents. The two endpoints of the noise-efficiency Pareto front at 21st generation are of particular interest and labelled as the "noise-optimal" design and "efficiency-optimal" design respectively. A total *PWL* reduction of 3.5dB has been obtained for the "noise-optimal" design of the present optimisation, accompanied by a 1.5% relative decrease of the pressure ratio and a 1.1% relative decrease of the mass flow. The "efficiency-optimal" design has achieved a maximum efficiency increase of 2.9%, but its pressure ratio and mass flow have dropped significantly by 4.8% and 3.7%. An overall trend of negative correlation observed in Fig. 9(c) further confirms the underlying competition between efficiency and pressure ratio. The nearly synchronised behaviour of pressure ratio and mass flow in Fig. 9(d) is a result of applying the working line constraint equation, i.e., Eqn. (4), during the optimisation.

4.2.2 Comparison of Rotor Characteristics

The rotor characteristics at the design speed for the "noise-optimal" design and the "efficiency-optimal" design are compared with the baseline results in Fig. 10. A clear penalty in pressure ratio characteristic can be seen for the "efficiency-optimal" design, whereas the "noise-optimal" design overall provides pressure ratios close to those of the datum blade. The increase in efficiency of each design is almost consistent over the range of mass flow rates rather than at a specific operating point. However, significant reductions of the stable operating range are observed for the two optimised blades. First, the choke mass flow rates are both reduced, which could make the two designs unusable for the take-off operation. This is mainly due to the working line constraint used during the optimisation, as going along the working line in the direction of reducing the pressure ratio, which usually reduces the blade loading, might be the "easiest" way to achieve efficiency gain and shock-associated noise reduction. It also can be seen that the operating point is driven by the optimiser to move from the $0.98\dot{m}_{\text{choke}}$ point to the peak efficiency point of the "efficiency-optimal" design, and the minimum noise point of the "noise-optimal" design (which will be seen in Fig. 11), respectively. This reduces the choke margin for each design and further contributes to the reduction of the choke mass flow. Second, clear reductions of the stall margin are also seen for the two designs. Note that the steady CFD divergence point is used in the present study only as a rough estimation, rather than a prediction, of the stall inception point to show how qualitatively the optimisation affects the stability of the rotor. The limited stable operating range of an optimised blade obtained using similar engineering parameter-based design space was also reported in previous studies [37, 38], which might suggest one disadvantage of this bulk-parameter type of design space.

The choke points for the two optimised designs can be recovered to the baseline level simply by opening up their blade passages. This is achieved by rotating the whole blade by certain degrees around the radial centreline, and the effects are noticeable as shown in Fig. 10. Meanwhile, only slight decreases in pressure ratio and efficiency are seen, which means from an engineering standpoint this way of choke-point recovery is useful. The characteristics of the two modified designs show that the rotor with lower compression ability is more efficient and has a larger stable operating range. Besides, the working line constraint offers the possibility to adjust the rotation speed to meet the specified thrust requirement if necessary.

4.2.3 Noise Performance

The noise performance results over the range of mass flow rates are shown in Fig. 11. It reveals the dependency between the total *PWL* and the mass flow on fixed speed lines of transonic rotors, i.e., reducing the mass flow would increase the noise power level at the inlet, except in the near choke region. First, throttling along the speed line would increase the blade loading, and the passage shock would gradually be expelled against the flow. It would merge with the oblique shock attached to the blade leading edge to form a strong bow shock which would be expelled further away from the blade. This forward movement of the shock structure effectively increases the near-field shock strength, in other words, the noise source level. Meanwhile, from the perspective of propagation, the reduction of the axial Mach number due to throttling would weaken the downstream convection effect of the mean flow. This reduces the so-called "time of flight" [1, 3] of an in-duct, helical wave over a fixed axial distance, which was known to be positively related to the amount of the nonlinear attenuation. Therefore, the reduction of attenuation during the shock wave propagation would

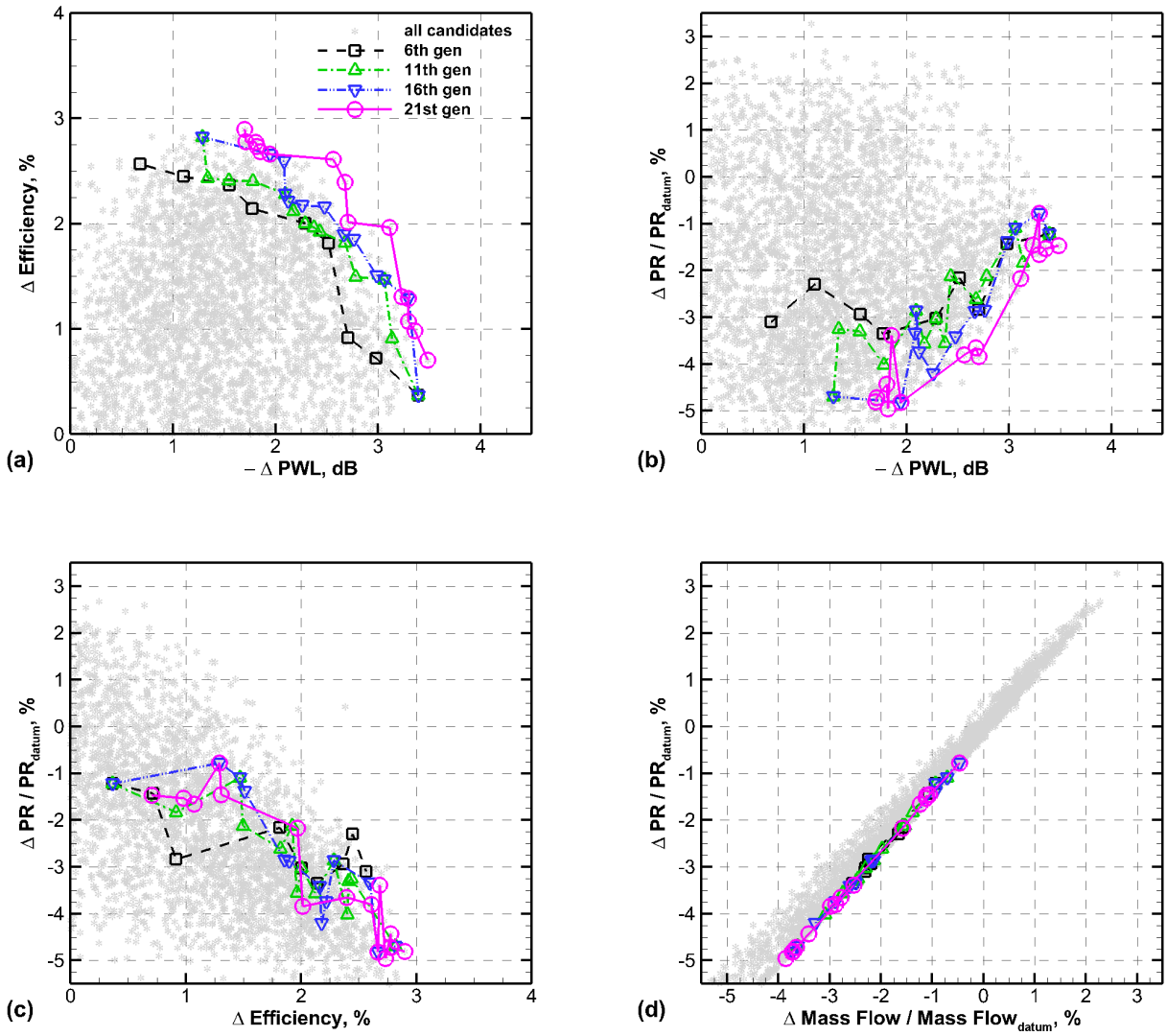

Fig. 9: Pareto-optimal solutions of the noise-efficiency optimisation

further increase the total *PWL* at the inlet.

The two optimised designs encouragingly show a similar noise reduction across their respective operating ranges. The noise reduction is seen to decrease slightly as the mass flow decreases. The two modified designs after the solid-body rotation for chokepoint recovery also show better noise performance than the datum blade across their operating ranges. Since the two modified designs now have the same choke point as the baseline rotor, it is reasonable to compare their flow fields at a given mass flow point to understand the mechanisms responsible for the performance improvements.

4.3 Analysis and Discussion

Numerical simulations at 98% of the choke mass flow corresponding to the design point of the datum blade, as indicated in Fig. 10 and 11, are carried out for the two choke-modified designs, which are labelled as the "noise-oriented" design and the "efficiency-oriented" design hereinafter.

4.3.1 Aerodynamics

Figure 12 compares the spanwise profiles of pressure ratio and efficiency between the "noise-oriented" design, the "efficiency-oriented" design, and the datum rotor at the same mass flow point. For the "noise-oriented" design, significant increases in pressure ratio around 60% span can be observed, while overall its efficiency profile is of minor difference from that of the datum rotor. The "efficiency-oriented" design exhibits significant increases in efficiency over the upper blade especially at 80% span, despite slight reductions below 40% span. However, clear reductions of pressure ratio above 10% span can be seen for the "efficiency-oriented" design.

The static pressure contours and the 2D blade profiles of the datum rotor and the "noise-oriented" design at 60% span in the blade-to-blade view are compared in Fig. 13. Clear backward sweep, more cambered aft section, and slight lean in the rotation direction, can be seen for the "noise-oriented" design in Fig. 13(c). Overall, the blade loading of the "noise-

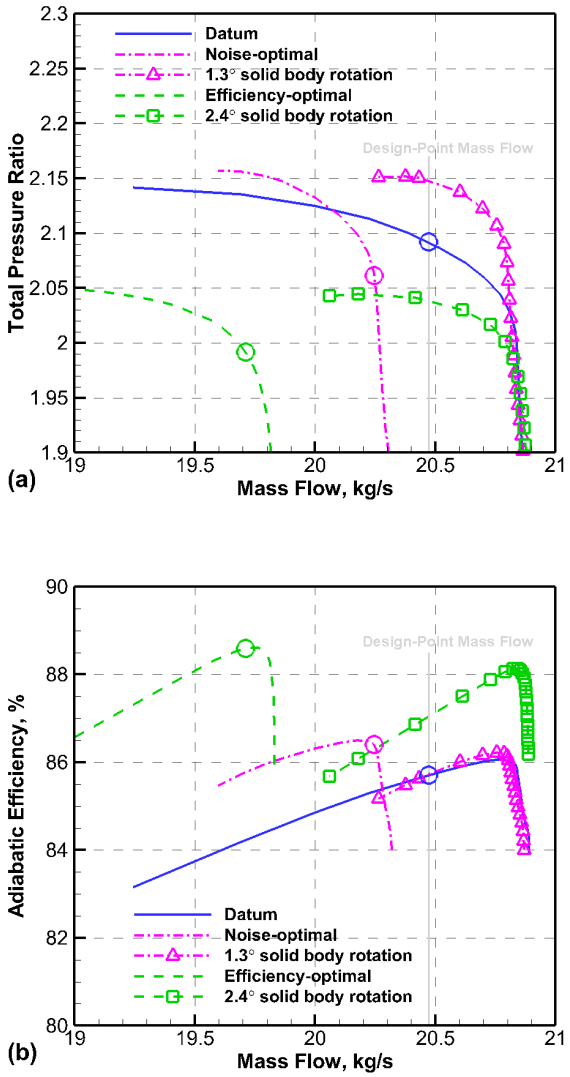

Fig. 10: Comparison of rotor performance curves of (a) total pressure ratio and (b) adiabatic efficiency between the baseline and two optimised blades (operating point represented by circles)

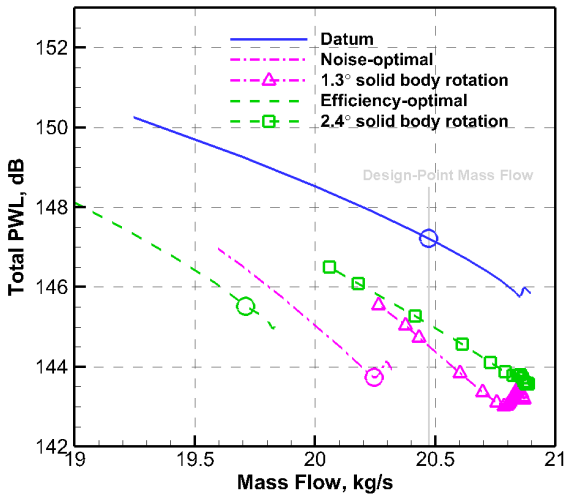

Fig. 11: Comparison of total *PWL* between the baseline and two optimised blades across their operating ranges (operating point represented by circles)

oriented" design at 60% span is increased due to a mild forward movement of the shock structure. Comparison of the pressure contours shows that, due to the backward sweep and lean, the passage shock and the leading-edge expansion fan are enhanced, and more suction is produced on the front part of the suction surface. It can be further confirmed from the blade loading distributions in Fig. 15(a), where a second supersonic expansion region is seen immediately following the suction peak on the suction surface of the "noise-oriented" blade. As a result, more pronounced front loading is produced. Figure 15(a) also indicates that a higher loading distribution in the mid-chord and rear-chord regions is produced by the "noise-oriented" design, which is due to more flow turning caused by the trailing edge re-cambering.

Figure 14 compares the relative Mach number contours and the 2D blade profiles of the datum rotor and the "efficiency-oriented" design at 80% span where the efficiency improvement is the most remarkable. The "efficiency-oriented" blade obviously has a larger chord than the datum. This increases the blade solidity locally, and in general, would reduce the blade loading and the shock strength. It also has other features like a forward-swept leading edge, a less cambered trailing edge, and an increased stagger angle (which would decrease the angle of attack). From the relative Mach number contours, it can be seen that a swallowed passage shock and a noticeable reduction of the shock-induced separation are produced by the "efficiency-oriented" shape. The blade loading distribution in Fig. 15(b) shows the pressure difference across the passage shock is reduced, and the shock is shifted downstream so that the separation on the suction side is delayed. As a result, both the shock loss and the viscous losses caused by shock-boundary layer interaction [4] are alleviated. Besides, it can be also seen that the front loading of the "efficiency-oriented" blade at 80% span is reduced.

In addition, it is found that the blade tip sections of the two choke-modified designs are both swept backwards and leant in the rotation direction compared with the tip section of the datum rotor. Therefore, similar to the previous analysis on how the blade shape at 60% span of the "noise-oriented" design affects the aerodynamics, these shape features lead to a forward movement of the shock and an increased front loading at the blade tip region for the two choke-modified designs. This implies a larger flow incidence and an enhanced tip leakage flow, and hence the stall margin is expected to be reduced [39].

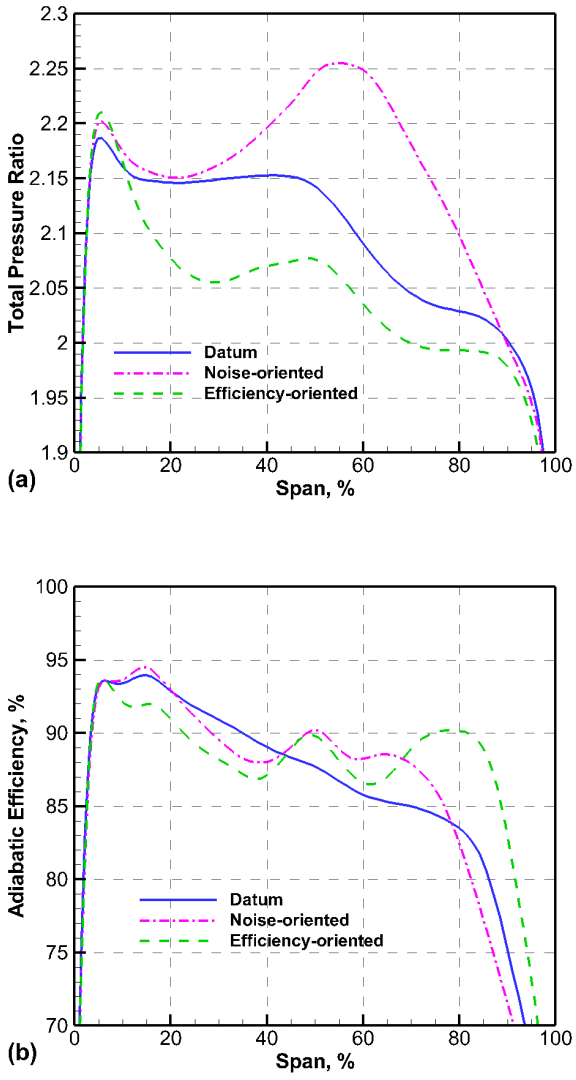

Fig. 12: Comparisons of spanwise performance profiles of (a) total pressure ratio and (b) adiabatic efficiency between the two choke-modified blades and the datum rotor at 98% of the choke mass flow

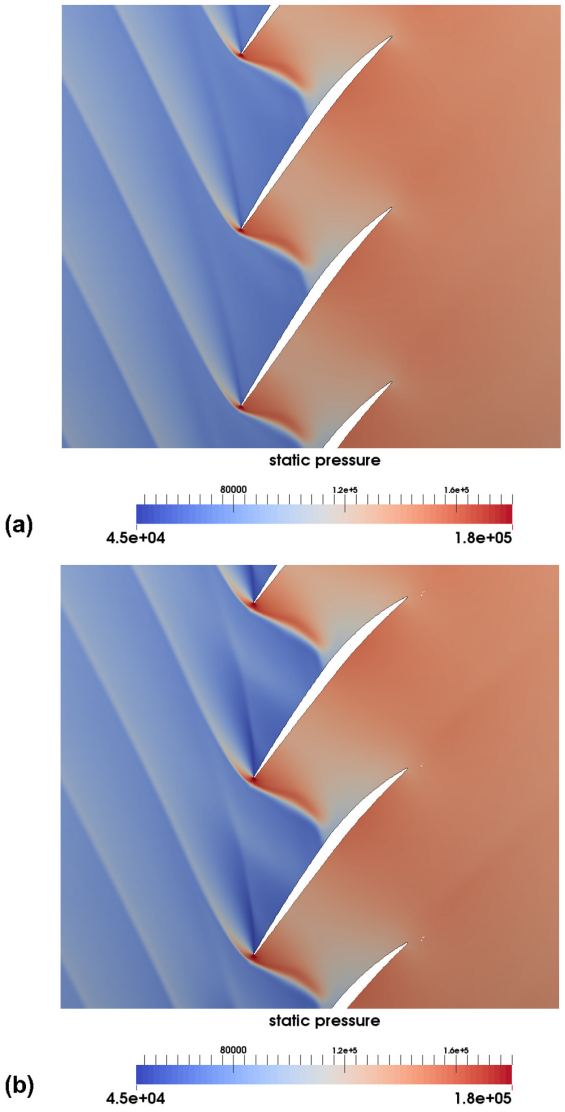

Fig. 13: Blade-to-blade views of static pressure contours for (a) the datum rotor and (b) the "noise-oriented" design at 60% span, and (c) comparison of the 2D blade sections

4.3.2 Noise Field

Figure 16 compares the pressure fields at the inlet between the two choke-modified blades and the datum rotor. It can be seen from Fig. 16(a) that the two designs both reduce the shock strength over the entire inlet plane. The shock waves are smeared near the inlet hub for the "efficiency-oriented" design, and it results in a significant reduction of the pressure fluctuations at 10% radial height. However, as shown in Fig. 16(c), the "noise-oriented" design exhibits more reduction of the pressure fluctuations at 70% radial height than the "efficiency-oriented" design. At 90% radial height, noise reductions achieved by the two optimised designs are close.

The rotor upstream acoustic fields for the datum blade and the two choke-modified designs are visualised in Fig. 17

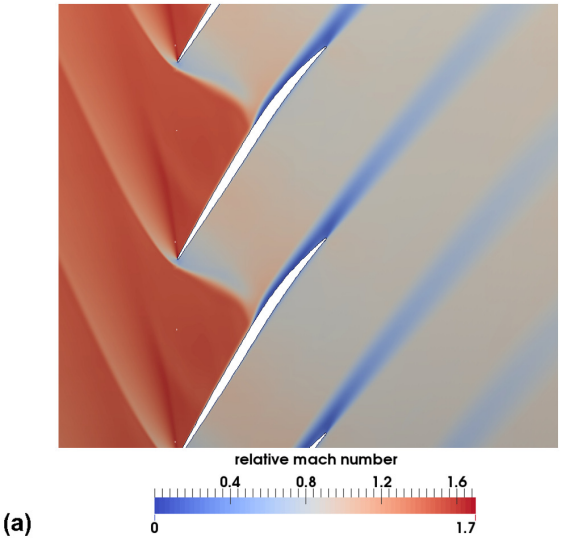

Fig. 14: Blade-to-blade views of relative Mach number contours for (a) the datum rotor and (b) the "efficiency-oriented" design at 80% span, and (c) comparison of the 2D blade sections

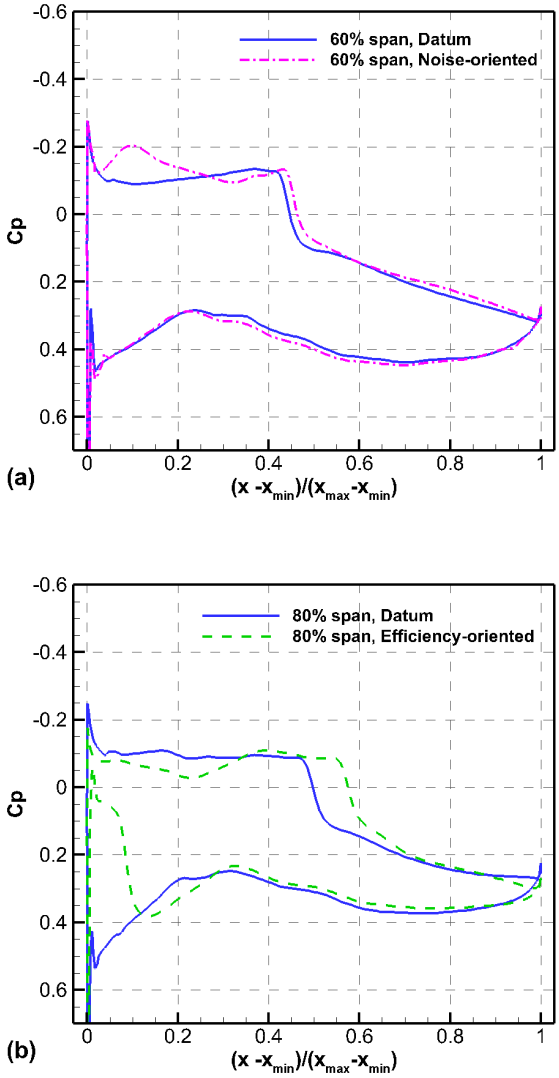

Fig. 15: Blade loading comparisons between the two choke-modified blades and the datum rotor at (a) 60% span and (b) 80% span

in terms of the root-mean-square (RMS) of the pressure fluctuations. Clearly, the two choke-modified designs have achieved noise reduction in the whole upstream region. They both eliminate the second hump around 80% radial height of the datum case near the rotor face, and the "noise-oriented" design shows a more radially localised noise source distribution. The shift of the primary bump from 25 to 70% radial height for each case as going upstream is caused by the 3D effect of mode shapes changing. Although the "efficiency-oriented" design is less noisy near the hub region (below 20% radial height) close to the inlet, the "noise-oriented" design produces more noise reduction in the upper half of the radial height. This makes the "noise-oriented" design exhibiting better noise performance in the light of acoustic power, as higher radial locations have larger weights in the acoustic power integration.

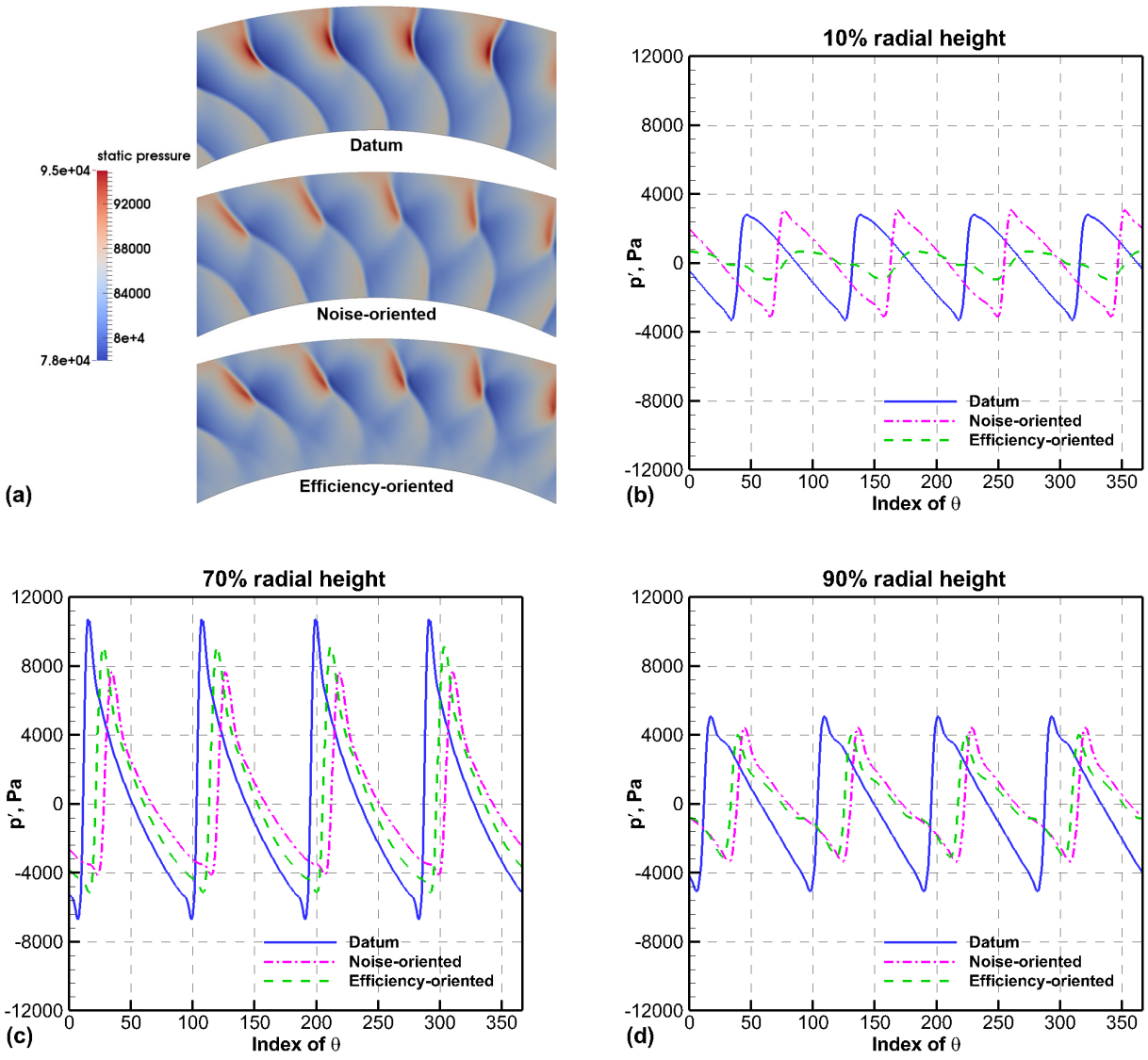

Fig. 16: Comparisons of (a) static pressure contours, and pressure fluctuation distributions at (b) 10% radial height, (c) 70% radial height, and (d) 90% radial height, of the domain inlet between the two choke-modified blades and the datum rotor

Wavesplitting analyses [25, 26] are conducted for the rotor upstream flow fields of the two choke-modified designs, and the *PWL* distributions of the first five upstream-propagating modes as well as the total net power for 1BPF are shown in Fig. 18. The upstream mean flow profiles for the two choke-modified blades and the datum rotor are slightly different, although the simulations are carried out at the same mass flow point. This means the eigenmodes are not identical for the three cases. Nonetheless, it can be seen in Fig. 18 and Fig. 5(a) that the behaviour of each individual mode of 1BPF is quite similar for the three cases except the fourth radial mode, which is seen to be largely suppressed by the "noise-oriented" design. However, the proportions in the total net power of each corresponding mode for the two choke-modified designs are clearly different.

5 Conclusions

In this paper, an aeroacoustic and aerodynamic automatic design optimisation of NASA rotor 37 was performed, using ARMOGA directly combined with three-dimensional, CFD-based analysis. The design goals were to reduce the shock-associated tone noise and to increase the adiabatic efficiency of the rotor. The noise-efficiency Pareto front obtained by ARMOGA demonstrated the trade-offs between the two objectives. The noticeable improvements for noise performance and efficiency of the Pareto optimal solutions, however, were accompanied by total pressure ratio reduction. Further analysis of rotor characteristics for the two endpoint Pareto optimal blades showed undesired reductions of the choke mass flow and the stall margin. Solid-body rotations were then applied to the optimised blades, and the choke points were successfully recovered to the baseline level. Compared with the datum rotor, the final "noise-

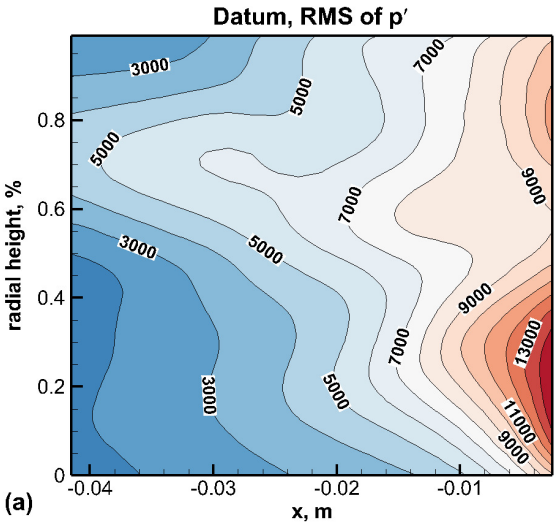

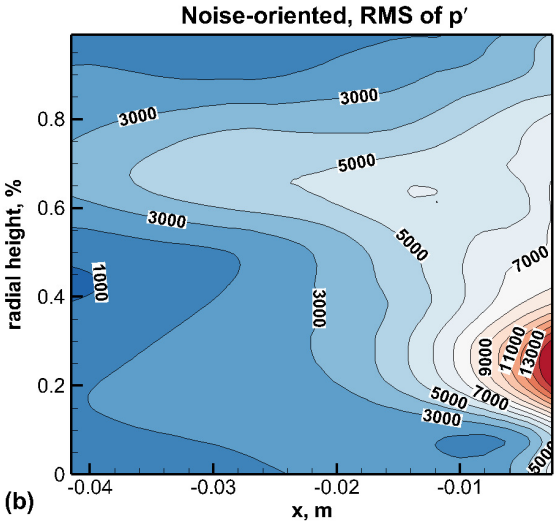

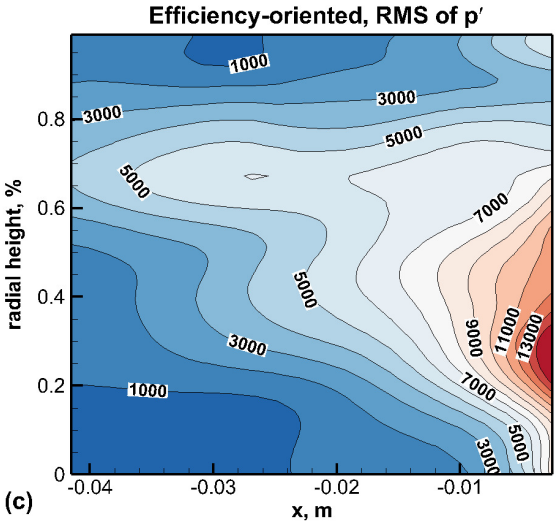

Fig. 17: RMS of pressure fluctuations for (a) the datum rotor, (b) the "noise-oriented" design, and (c) the "efficiency-oriented" design at 98% of the choke mass flow

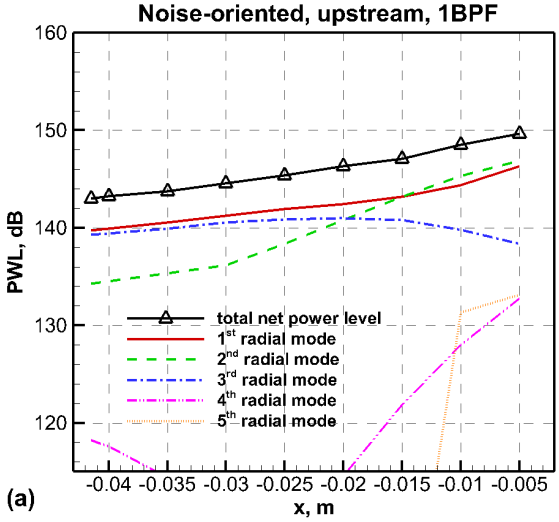

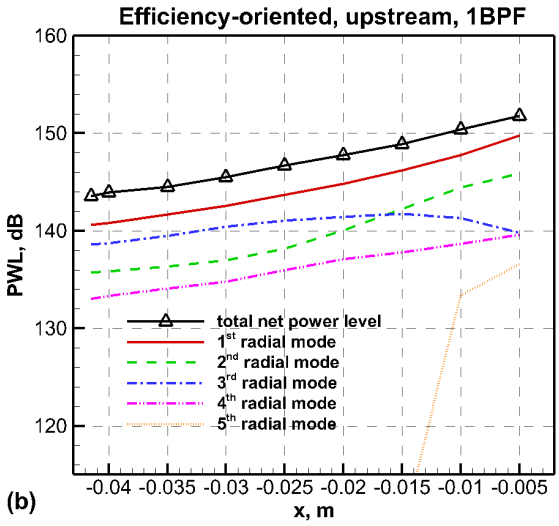

Fig. 18: Axial distributions of *PWL* of upstream-propagating modes as well as the total net power for 1BPF for (a) the "noise-oriented" design and (b) the "efficiency-oriented" design

oriented" design exhibited lower acoustic power level, higher total pressure ratio, and almost the same efficiency across the operating range at the design speed. And yet the "efficiency-oriented" design showed depressed acoustic power level, increased efficiency, and decreased total pressure ratio.

Based on the comparison of spanwise performance profiles, it was found that the flow field around 60% span contributed most to the total pressure ratio increase for the "noise-oriented" design. The shock wave, as well as the expansion fan, was enhanced and the blade loading was increased, due to the backwards swept and leant, more cambered blade sectional profile. For the "efficiency-oriented" design, the efficiency increase was mainly attributed to the improvement of the flow field around 80% span. At this location shock loss and viscous losses generated by shock-

boundary layer interaction were both reduced, as a result of higher solidity blades with forward-swept leading edges, less cambered trailing edges, and increased stagger angles.

The three-dimensional effect of the axial change of radial mode shapes might play a role in the nonlinear propagation of shock waves for the present case. Compared with the datum rotor, the two choke-modified designs both showed better noise performance across their whole operating ranges. The two choke-modified designs changed the noise source distribution near the rotor face, from a double-hump pattern over the entire radial height to a single hump located in the lower radial region. This led to noise reduction in the rotor upstream region. It was demonstrated that the aeroacoustic and aerodynamic performance of NASA rotor 37 can be simultaneously improved by the automatic MDO approach.

Further efforts can be made to include the blade mechanical analysis in the optimisation. Besides, it is necessary to perform multipoint optimisations to achieve more robust blade designs that would meet the various, real-world design requirements. The global-search optimisation in this paper can also be combined with the adjoint gradient-based optimisation to develop a hybrid strategy for large-scale MDO problems in turbomachinery.

Acknowledgements

This work is funded by the MADELEINE project from the European Union's Horizon 2020 research and innovation programme under grant agreement No. 769025. Also, the authors acknowledge Rolls-Royce's support for the computing facility and software used in this work.

References

[1] Morfey, C. L., and Fisher, M. J., 1970. "Shock-wave radiation from a supersonic ducted rotor". *The Aeronautical Journal of the Royal Aeronautical Society,* **74**(715), pp. 579–585.

[2] Morfey, C. L., 1964. "Rotating pressure patterns in ducts: Their generation and transmission". *Journal of Sound and Vibration,* **1**(1), pp. 60–87.

[3] McAlpine, A., and Fisher, M. J., 2001. "On the prediction of "buzz-saw" noise in aero-engine inlet ducts". *Journal of Sound and Vibration,* **248**(1), pp. 123–149.

[4] Denton, J. D., 1993. "The 1993 igti scholar lecture: Loss mechanisms in turbomachines". *ASME Journal of Turbomachinery,* **115**(4), pp. 621–656.

[5] Deb, K., Pratap, A., Agarwal, S., and Meyarivan, T., 2002. "A fast and elitist multiobjective genetic algorithm: Nsga-ii". *IEEE Transactions on Evolutionary Computation,* **6**(2), pp. 182–197.

[6] Sasaki, D., and Obayashi, S., 2005. "Efficient search for trade-offs by adaptive range multi-objective genetic algorithms". *Journal of Aerospace Computing, Information, and Communication,* **2**(1), pp. 44–64.

[7] Lian, Y., and Liou, M. S., 2005. "Multiobjective optimization using coupled response surface model and evolutionary algorithm". *AIAA Journal,* **43**(6), pp. 1316–1325.

[8] Pierret, S., Coelho, R. F., and Kato, H., 2007. "Multidisciplinary and multiple operating points shape optimization of three-dimensional compressor blades". *Structural and Multidisciplinary Optimization,* **33**(1), pp. 61–70.

[9] Shahpar, S., 2004. "Design of experiment, screening and response surface modelling to minimise the design cycle time". *VKI Lecture Series on Optimisation Methods and Tools for Multicriteria/Multidisciplinary Design*, pp. 1–49.

[10] Samad, A., Kim, K. Y., Goel, T., and Haftka, R. T., 2008. "Multiple surrogate modeling for axial compressor blade shape optimization". *AIAA Journal of Propulsion and Power,* **24**(2), pp. 301–310.

[11] Benini, E., 2004. "Three-dimensional multi-objective design optimization of a transonic compressor rotor". *AIAA Journal of Propulsion and Power,* **20**(3), pp. 559–565.

[12] Ellbrant, L., Eriksson, L. E., and Mårtensson, H., 2012. "Design of compressor blades considering efficiency and stability using cfd based optimization". In Proceedings of the ASME Turbo Expo 2012: Turbine Technical Conference and Exposition, Vol. **8** of *Turbomachinery, Parts A, B, and C*, ASME, pp. 371–382. See also URL `https://doi.org/10.1115/GT2012-69272`.

[13] Luo, C., Song, L., Li, J., and Feng, Z., 2012. "A study on multidisciplinary optimization of an axial compressor blade based on evolutionary algorithms". *ASME Journal of Turbomachinery,* **134**(5), p. 054501.

[14] Baert, L., Beaucaire, P., Leborgne, M., Sainvitu, C., and Lepot, I., 2017. "Tackling highly constrained design problems: Efficient optimisation of a highly loaded transonic compressor". In Proceedings of the ASME Turbo Expo 2017: Turbomachinery Technical Conference and Exposition, Vol. **2C** of *Turbomachinery*, ASME. See also URL `https://doi.org/10.1115/GT2017-64610`.

[15] Polynkin, A., Toropov, V., and Shahpar, S., 2010. "Multidisciplinary optimization of turbomachinary based on metamodel built by genetic programming". In 13th AIAA/ISSMO Multidisciplinary Analysis Optimization Conference, AIAA. AIAA 2010-9397.

[16] Wilson, A. G., Stieger, R., Coupland, J., Smith, N. H., and Humphreys, N. D., 2011. "Multi-disciplinary optimisation of a transonic fan for low tone noise". In 17th AIAA/CEAS Aeroacoustics Conference (32nd AIAA Aeroacoustics Conference), AIAA. AIAA 2011-2950.

[17] Shahpar, S., CIMNE, 2002. "Soft: A new design and optimisation tool for turbomachinery". *Evolutionary Methods for Design, Optimisation and Control*.

[18] Denton, J. D., 1997. "Lessons from rotor 37". *Journal of Thermal Science,* **6**(1), pp. 1–13.

[19] Ameri, A., 2009. "Nasa rotor 37 cfd code validation glenn-ht code". In 47th AIAA Aerospace Sciences Meeting including The New Horizons Forum and Aerospace Exposition, AIAA. AIAA 2009-1060.

[20] Dunham, J., 1998. CFD Validation for Propulsion System Components. Tech. rep., Advisory Group for Aerospace Research and Development (AGARD), Neuilly-Sur-Seine, France, May.

[21] Reid, L., and Moore, R., 1978. Design and Overall Performance of Four Highly Loaded, High-Speed Inlet Stages for an Advanced High-Pressure Ratio Core Compressor. Tech. rep., October. NASA-TP-1337.

[22] Suder, K. L., 1996. Experimental Investigation of the Flow Field in a Transonic, Axial Flow Compressor with Respect to the Development of Blockage and Loss. Tech. rep. NASA-TM-107310.

[23] Hawkings, D., 1972. Transonic Fan Noise. Tech. rep., Ministry of Defence (Procurement Executive), Aeronautical Research Council, March. CP No. 1226: 1–11.

[24] Lapworth, L., 2004. "Hydra-cfd : A framework for collaborative cfd development". In International Conference on Scientific and Engineering Computation (ICSEC).

[25] Wilson, A. G., 2001. "A method for deriving tone noise information from cfd calculations on the aero-engine fan stage". In NATO RTO-AVT Symposium on Developments in Computational Aero- and Hydro-Acosutics.

[26] Moinier, P., and Giles, M. B., 2005. "Eigenmode analysis for turbomachinery applications". *AIAA Journal of Propulsion and Power,* **21**(6), pp. 973–978.

[27] Morfey, C. L., 1971. "Acoustic energy in non-uniform flows". *Journal of Sound and Vibration,* **14**(2), pp. 159–170.

[28] Shahpar, S., and Lapworth, L., 2003. "Padram: Parametric design and rapid meshing system for turbomachinery optimisation". In Proceedings of the ASME Turbo Expo 2003, collocated with the 2003 International Joint Power Generation Conference, Vol. **6** of *Turbo Expo 2003, Parts A and B*, ASME, pp. 579–590. See also URL `https://doi.org/10.1115/GT2003-38698`.

[29] Wilson, A. G., and Coupland, J., 2004. "Numerical prediction of aeroengine fan stage tone noise sources using cfd". In Proceedings of the European Congress on Computational Methods in Applied Sciences and Engineering.

[30] Chima, R., 2009. "Swift code assessment for two similar transonic compressors". In 47th AIAA Aerospace Sciences Meeting including The New Horizons Forum and Aerospace Exposition, AIAA. AIAA 2009-1058.

[31] Seshadri, P., Parks, G. T., and Shahpar, S., 2015. "Leakage uncertainties in compressors: The case of rotor 37". *AIAA Journal of Propulsion and Power,* **31**(1), pp. 456–466.

[32] Cumpsty, N. A., 2010. "Some lessons learned". *ASME Journal of Turbomachinery,* **132**(4), p. 041018.

[33] Shabbir, A., Celestina, M. L., Adamczyk, J. J., and Strazisar, A. J., 1997. "The effect of hub leakage flow on two high speed axial compressor rotors". In Proceedings of the ASME 1997 International Gas Turbine and Aeroengine Congress and Exhibition, Vol. **1** of *Aircraft Engine; Marine; Turbomachinery; Microturbines and Small Turbomachinery*, ASME. See also URL `https://doi.org/10.1115/97-GT-346`.

[34] Fink, M. R., 1971. "Shock wave behavior in transonic compressor noise generation". *ASME Journal of Engineering for Power,* **93**(4), pp. 397–403.

[35] Leary, S., Bhaskar, A., and Keane, A., 2003. "Optimal orthogonal-array-based latin hypercubes". *Journal of Applied Statistics,* **30**(5), pp. 585–598.

[36] Shahpar, S., 2005. "Sophy: An integrated cfd based automatic design optimization system". Paper No. ISABE-2005-1086.

[37] Brooks, C., Forrester, A., Keane, A., and Shahpar, S., 2011. "Multifidelity design optimization of a transonic compressor rotor". In Proceedings of the 9th European Conference on Turbomachinery Fluid Dynamics and Thermodynamics, Vol. **2**, pp. 1267–1276.

[38] Shahpar, S., Polynkin, A., and Toropov, V., 2008. "Large scale optimization of transonic axial compressor rotor blades". In Proceedings of the 49th AIAA/ASME/ASCE/AHS/ASC Structures, Structural Dynamics, and Materials Conference. AIAA 2008-2056.

[39] Denton, J. D., 2002. "The effects of lean and sweep on transonic fan performance, a computational study". *Task Quarterly,* **6**(1), pp. 7–23.